Journal of Energy Storage 58 (2023) 106312

Contents lists available at ScienceDirect

Journal of Energy Storage

journal homepage: www.elsevier.com/locate/est

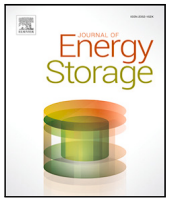

Research papers

Melting control of phase change material of semi-cylinders inside a horizontal baffled channel: Convective laminar fluid–structure interaction

Salah M. Salih [a], Ammar I. Alsabery [b,*], Ahmed K. Hussein [c], Muneer A. Ismael [d], Mohammad Ghalambaz [e], Ishak Hashim [f]

[a] Engineering Technical College of Al-Najaf, Al-Furat Al-Awsat Technical University, Kufa, Iraq
[b] Refrigeration & Air-conditioning Technical Engineering Department, College of Technical Engineering, The Islamic University, Najaf, Iraq
[c] Mechanical Engineering Department, College of Engineering, University of Babylon, Babylon City, Hilla, Iraq
[d] Mechanical Engineering Department, Engineering College, University of Basrah, Basrah, Iraq
[e] Laboratory on Convective Heat and Mass Transfer, Tomsk State University, Tomsk 634045, Russia
[f] Department of Mathematical Sciences, Faculty of Science & Technology, Universiti Kebangsaan Malaysia, 43600 UKM Bangi, Selangor, Malaysia

ARTICLE INFO

Keywords:
Two alternative PCMs
Heat transfer enhancement
Flexible baffles
Fluid–structure interaction (FSI)
Horizontal channel
Semi cylinders

ABSTRACT

The problem studied in this paper consists of forced fluid flow inside a horizontal channel involving two semi-cylinders and two flexible baffles attached alternatively to the lower and upper walls of the channel. A phase change material fills the semi-cylinders, which are being heated by constant temperature. Cold air is forced through the channel to induce the contributions of convective and conductive heat transfers, fluid–structure interaction and the melting of phase change material. The prevailing mathematical equations of these physics are normalized and solved using the finite element method with the ALE scheme. The influential parameters are: dimensionless time τ, the elasticity modulus of the baffles E and the Reynolds number Re. The most important results show a retardation of melting volume fraction with increasing Reynolds number and decreasing the elasticity modulus of the flexible baffles. It is found that elevating Re from 10 to 500 and E from 5×10^4 to 5×10^6, the melting volume fraction MVF at $\tau = 15$ reduces by 4.15% and increases by 5.2%, respectively. The flexible baffles having a lower modulus of elasticity augment the Nusselt number very slightly (0.9%), while the pressure drop along the channel decreases notably.

1. Introduction

Storage of alternative energy sources is significant for regulating the mismatch between the consumed and demanded energy in time for systems to operate more effectively and reliably. Over the past two decades, researchers have focused on using phase change materials (PCMs) as latent thermal energy storage (LTES) instead of sensible thermal energy storage (STES). This can be attributed to a solid–liquid PCM capability of periodically absorbing, storing, and releasing thermal energy in the form of latent heat during phase change for charging/discharging periods under the nearly isothermal system. During the phase transition of materials, thermal energy is stored when they melt, and it is recovered when they solidify [1]. Hence, LTES is considered more attractive for various engineering applications, including climate control of domestics, drying of industrial and agricultural products, and water desalination [2–6].

Despite the high storage capacity of LTES of gained energy during the melting time, its melting/solidification rates in the system are still low due to the poor PCM conductivity and the energy exchange rate between the fluid streams and the paraffin wax layers into containers of storage. Several studies have employed various technologies for improving the effective thermal conductive rate, such as nanoparticle-paraffin wax [7–9], PCM encapsulation [10–12], multi-PCM [13–15], porous metal foam [16–18], and fins structure [19,20]. Utilizing fins in the LTES units gives better enhancement than nanotechnology [21].

Numerical optimization of PCM with fins in heat sinks was achieved by Pakrouh et al. [22]. They concluded that the optimum PCM percentage was highly influenced by the fin parameters, such as number, height, and thickness. Arshad et al. [19] investigated the cooling enhancement of electronic devices' performance experimentally using different thicknesses of aluminum pins in PCM enclosures. They concluded that the optimum efficiency of the system was reached for a 2 mm thick finned-PCM heat sink.

Bhagat et al. [23] analyzed numerically the solar thermal storage utilizing PCM, the influence of fin parameters on the PCM layer, and

* Corresponding author.
E-mail address: ammar_e_2011@yahoo.com (A.I. Alsabery).

https://doi.org/10.1016/j.est.2022.106312
Received 14 July 2022; Received in revised form 14 November 2022; Accepted 2 December 2022
Available online 14 December 2022

Nomenclature

C	Elasticity tensor
d_s	Displacement vector
E	Dimensional Young's modulus of the flexible wall
F_v	Body force vector in the elastic wall
h	The height of the channel
k	Thermal conductivity
K_r	Thermal conductivity ratio
L_{PCM}	Latent heat of the PCM
n	Unit normal vector
Nu	Nusselt number
P	Dimensionless pressure
Pr	Prandtl number
Re	Reynolds number
s	Phase change function
S	Piola–Kirchhoff stress tensor
Ste	Stefan number
T	Temperature
u	Fluid velocity vector
w	Coordinates velocity vector

Greek symbols

α	Thermal diffusivity
β	Thermal expansion coefficient
ε	Strain rate
θ	Dimensionless temperature
ν	Poisson's ratio
ρ	Density
σ	Stress tensor
τ	Dimensionless time
ψ	Stream function

Super subscripts

$*$	Dimensional
T	Transpose

Subscript

f	Fluid, fusion
h	Hot
in	Inlet
l	Liquid
out	Outlet
PCM	Phase change material
r	Ratio
s	Solid

heat transfer fluid (HTF) streams during melting/solidification periods. The results showed a reduction in the temperature variation of HTFs. A mathematical model of encapsulated-paraffin wax as a TES unit for different geometry of the ventilation flow was evaluated by Zukowski [24]. He observed that the charge/discharge time depends on the geometry dimensions and paraffin density.

The aspect of heat transfer enhancement with turbulators and vortex flow devices of the internal duct/channel has been reported by recent investigators. Verma et al. [25] simulated the transient thermal performance of a solar air heater with embedded PCMs. In their design, the receiver medium is made of a PCM container, and air flows between the glass cover and the PCM received. They concluded that the PCM could provide an excellent thermal backup and reported a potential thermal efficiency of up to 63%. Promvonge et al. [26] examined the impact of a novel design of longitudinal-vortex generators on solar absorber performance. They showed that a novel design could provide a heat transfer rate several times greater than traditional smooth designs with a cost of increased friction. In another study, Zahran et al. [27] employed a channel with a corrugated surface to increase the heat transfer rate in a channel flow. They examined the effect of channel wall corrugation for various Reynolds numbers. The results showed that a corrugated surface could enhance the heat transfer for all investigated cases with a drawback of a slight increase in the pressure drop. Then, the authors addressed the impact of corrugated geometry on heat transfer enhancement and found up to 1.5 times the heat transfer enhancement factor for an optimum design of a corrugated surface. Thus, a corrugated surface was proposed as an effective means for heat transfer enhancement in air ducts. Wang et al. [28] examined the impact of turbulators on the heat transfer enhancement of serpentine channels with the pulsating flow and heat transfer. They employed winglike turbulators to enhance the heat transfer rate. Their results showed that the flow pulsation effects could enhance the heat transfer rate by 13% compared to a steady-state flow. They also reported that tilde-like turbulators could result in a thermal performance factor of 1.39.

The literature review shows some research studies utilized PCM containers as channel walls to enhance the heat transfer and thermal stability of heating air flows. Some researchers utilized obstacles such as turbulators and wavy surface methods to enhance the heat transfer rate in channels. However, no study addressed the impact of utilizing PCM obstacles and flexible baffles on the heat transfer in channels. In the present work, we analyze the use of two alternative PCMs obstacles enclosed by a semi-cylinder (semicircle) with two flexible baffles to direct the heat transfer fluid with less pressure drop for the first time. The idea behind the present geometry is to utilize the latent heat stored in the phase change PCM material to remove the heat from a hot segment. The PCM containers are designed as a semicircle (cross-sectional) to reduce the separation of streamlines of the cooling air and reduce the total pressure drop. Two flexible baffles are added to direct the cooling air towards the PCM container with less pressure drop.

2. Mathematical formulation

Consider 2-dimensional transient forced convection flow and heat transfer within a channel with height h (where $h = 0.6$) and length of L ($L = 10$ h) (see Fig. 1). Two flexible baffles sections are embedded into the top and bottom surfaces of the channel over a length of 0.5 h. These segments are considered very thin with a thickness of 0.012 h and elasticity modulus E^*. The function of these two flexible segments is to direct the flow over two semicircular enclosures attached alternatively on the horizontal walls of the channel. These enclosures involve phase change materials and their walls are considered to be of very high thermal conductivity. The diameter of each enclosure is equal to h and aligned with the wall of the channel and heated by T_h. Fluid flow is considered incompressible air. By neglecting the buoyancy force within the channel, all physical properties of the fluid and the flexible wall are assumed unchanged. The dimensional unsteady governing equations of the laminar fluid classified into vector form in the Arbitrary Lagrangian–Eulerian procedure (ALE) are written as:

$$\nabla \cdot u^* = 0, \tag{1}$$

$$\frac{\partial u^*}{\partial t^*} + (u^* - w^*) \cdot \nabla u^* = -\frac{1}{\rho_f}\nabla p + \frac{1}{\rho_f}\nabla^2 u^*, \tag{2}$$

$$\frac{\partial T^*}{\partial t^*} + (u^* - w^*) \cdot \nabla T^* = \alpha_f \nabla^2 T^*, \tag{3}$$

where u^* is the fluid velocity vector, w^* is the moving coordinate velocity, ρ_f the fluid density and T^* is the dimensional temperature.

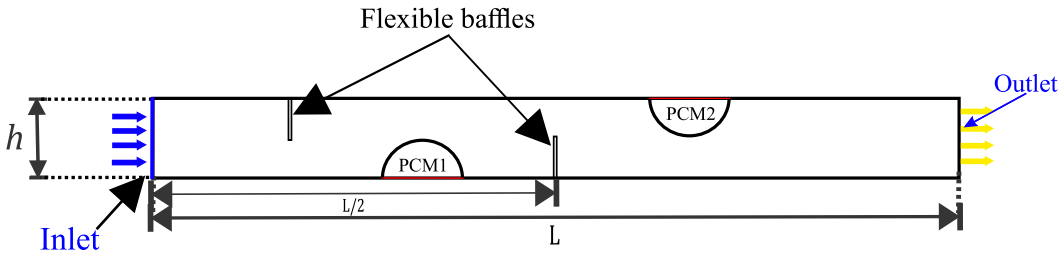

Fig. 1. 2D schematic diagram of the physical model.

The dimensional unsteady governing equations concerning the flexible portion are arranged within a vector pattern as follows:

$$\rho_s \frac{d^2 \mathrm{d}_s^*}{dt^{*2}} - \nabla\sigma^* = \mathrm{F}_\mathrm{v}^*, \tag{4}$$

$$\frac{\partial T^*}{\partial t^*} = \alpha_s \nabla^2 T^*, \tag{5}$$

where ρ_s, σ^*, d_s^*, F_v^* and α_s are the solid density, stress tensor, solid displacement vector, applied body force and thermal diffusivity of solid respectively. Considering the wall is linearly elastic, the stress tensor is:

$$\sigma = J^{-1} F S F^T, \quad F = (1 + \nabla_s^*), \quad J = \det(F). \tag{6}$$

The second Piola–Kirchhoff stress tensor is $S = C : (\varepsilon)$, where $\varepsilon = \frac{(\nabla \mathrm{d}_s^* + \nabla \mathrm{d}_s^{*T} + \nabla \mathrm{d}_s^{*T} \cdot \nabla \mathrm{d}_s^*)}{2}$ and $C = C(E^*, \nu)$.

The conduction heat transfer in the PCM regions is governed by the conservation of energy as follows:

$$\left(\rho_{PCM} C_{PCM}\right) \frac{\partial T^*}{\partial t^*} = \nabla\left(k_{PCM} \nabla T^*\right) + \rho_{PCM} L_{PCM} \frac{\partial s^*(T^*)}{\partial t^*}, \tag{7}$$

where the subscript of PCM denotes the PCM thermophysical properties, and L_{PCM} is the latent heat of phase change. The phase change function s^* is introduced as follows:

$$s^*\left(T^*\right) = \begin{cases} 0, & T^* < T_f - \frac{\delta T}{2}, \\ \frac{T^* - T_f}{\delta T} + \frac{1}{2}, & T_f - \frac{\delta T}{2} < T^* < T_f + \frac{\delta T}{2}, \\ 1, & T^* > T_f + \frac{\delta T}{2}. \end{cases} \tag{8}$$

Here, T_f is the fusion temperature of PCM and δT is the phase change interval. The thermophysical properties of the solid and liquid PCM are different, and hence the effective thermophysical properties as a function of temperature are calculated as:

$$(\rho C)_{PCM} = (\rho C)_{s,PCM}\left(1 - s^*\left(T^*\right)\right) + (\rho C)_{l,PCM} s^*\left(T^*\right), \tag{9}$$

$$k_{PCM} = k_{s,PCM}\left(1 - s^*\left(T^*\right)\right) + k_{l,PCM} s^*\left(T^*\right), \tag{10}$$

where the subscripts s and l indicate the solid and liquid PCM thermophysical properties, respectively.

On the flexible surfaces and the PCM-fluid interface we have the following conditions

$$\frac{\partial \mathrm{d}_s^*}{\partial t^*} = u^*, \quad \sigma^* \cdot n^* = -p + \mu^* \nabla u^*, \quad k_f \frac{\partial T^*}{\partial n^*} = k_s \frac{\partial T^*}{\partial n^*}, \quad k_f \frac{\partial T^*}{\partial n^*} = k_{PCM} \frac{\partial T^*}{\partial n^*}. \tag{11}$$

Using the dimensionless variables

$$(X, Y) = \frac{x, y}{L}, \; H = \frac{h}{L}, \; (u, v) = \frac{(u^*, v^*)}{u_{\mathrm{in}}}, \quad \theta = \frac{T^* - T_{\mathrm{in}}}{T_f - T_{\mathrm{in}}}, \; \mathrm{d}_s = \frac{\mathrm{d}_s^*}{L}, \; \sigma = \frac{\sigma^*}{E^*}, \; \tau = \frac{t^* \alpha_f}{L^2}, \; P = \frac{p}{\rho_f u_{\mathrm{in}}^2}, \tag{12}$$

gives

$$\nabla \cdot u = 0, \tag{13}$$

$$\frac{\partial u}{\partial \tau} + (u - w) \cdot \nabla u = -\nabla P + \frac{1}{Re} \nabla^2 u, \tag{14}$$

$$\frac{\partial \theta}{\partial \tau} + (\mathrm{u} - w) \cdot \nabla \theta = \frac{1}{Re \cdot \mathrm{Pr}} \nabla^2 \theta, \tag{15}$$

$$\frac{1}{\rho_r} \frac{d^2 \mathrm{d}_s}{dt^2} - E \cdot \nabla\sigma = E \cdot \mathrm{F}_\mathrm{v}, \tag{16}$$

$$\frac{\partial \theta}{\partial \tau} = \alpha_r \cdot \nabla^2 \theta, \tag{17}$$

$$\left(\frac{\rho_{PCM} C_{PCM}}{\rho_f C_f}\right) \frac{\partial \theta}{\partial \tau} = \nabla\left(\left(\frac{k_{PCM}}{k_f}\right) \nabla\theta\right) + \left(\frac{\rho_{PCM}}{\rho_f}\right) \frac{1}{Ste} \frac{\partial s(\theta)}{\partial t}, \tag{18}$$

where $Re = \frac{u_{\mathrm{in}} L}{\nu_f}$ is Reynolds number, $\mathrm{Pr} = \frac{\nu_f}{\alpha_f}$ is the Prandtl number, $E = \frac{E^* L^2}{\rho_f \alpha_f^2}$ is the flexibility parameter, $\rho_r = \frac{\rho_f}{\rho_s}$, $\alpha_r = \frac{\alpha_f}{\alpha_s}$ are the thermal diffusivity ratio and the density ratio parameter, $Ste = \frac{C_f (T_f - T_{\mathrm{in}})}{L_{PCM}}$ is the Stefan number.

Initially, the channel is connected to hot top and bottom segments attached to the horizontal surfaces and cold inlet velocity, and the fluid is quiescent (i.e. $u^* = 0$). The dimensionless boundary conditions of Eqs. (13)–(18) are:

On the inlet boundary: $u = (1, 0), \; \theta = 0,$ (19)

On the outlet boundary: $P = 0,$ (20)

On the heated parts of the bottom and top boundaries: $\theta = 1,$ (21)

On the solid adiabatic (No slip condition) boundaries:

$$u = v = 0, \; \nabla\theta = 0, \tag{22}$$

On the interface between fluid and flexible segments:

$$\left(\frac{\partial \theta}{\partial n}\right) = K_r \left(\frac{\partial \theta_s}{\partial n}\right), \tag{23}$$

$$\frac{\partial \theta}{\partial n} = \left(\frac{k_{PCM}}{k_f}\right) \frac{\partial \theta}{\partial n}, \tag{24}$$

where $K_r = \frac{k_s}{k_f}$. Also, on the solid-fluid interface we have

$$\frac{\partial \mathrm{d}_s}{\partial \tau} = u \text{ and } \frac{E}{\rho_f u_{\mathrm{in}}^2} \sigma \cdot \mathrm{n} = -P + \frac{D_{ij}}{Re} \nabla \mu_a. \tag{25}$$

The dimensionless initial temperature at the fluid and the fin is $\theta = 0.5$. The dimensionless initial velocity is $u = 0$. For the pressure point constraint, the following dimensionless pressure constraint is also considered:

$$P = 0. \tag{26}$$

The non-dimensional form of the phase change source term is

$$s(\theta) = \begin{cases} 0, & \theta < -\frac{1}{2}, \\ \frac{\theta}{\delta\theta} + \frac{1}{2}, & -\frac{1}{2} < \theta < +\frac{1}{2}, \\ 1, & \theta > +\frac{1}{2}, \end{cases} \tag{27}$$

where $\delta\theta = \delta T / \left(T_f - T_{\mathrm{in}}\right)$.

The non-dimensional thermophysical ratios are also introduced as follows:

$$\frac{(\rho C)_{PCM}}{(\rho C)_f} = \frac{(\rho C)_{s,PCM}}{(\rho C)_f}(1 - s(\theta)) + \frac{(\rho C)_{l,PCM}}{(\rho C)_f} s(\theta), \tag{28}$$

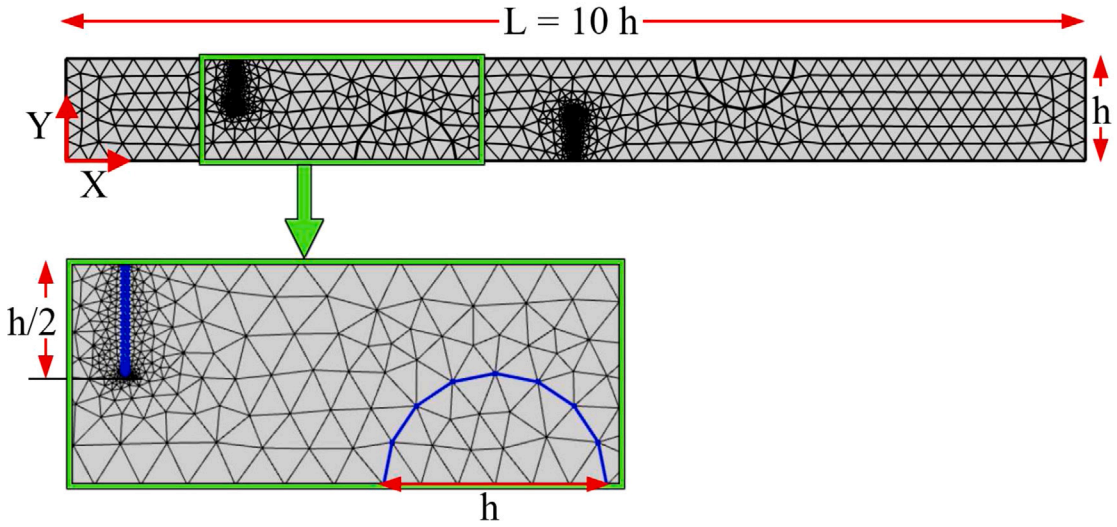

Fig. 2. Grid-points distribution with 2936 elements. Mesh consists of 2936 elements. Minimum quality: 0.5667; average quality: 0.8484.

$$\frac{k_{PCM}}{k_f} = \frac{k_{s,PCM}}{k_f}(1 - s(\theta)) + \frac{k_{l,PCM}}{k_f} s(\theta). \tag{29}$$

Here, $\frac{k_{l,PCM}}{k_f} = 0.267$, $\frac{k_{s,PCM}}{k_f} = 0.366$, $\frac{(\rho C)_{s,PCM}}{(\rho C)_f} = 0.920$, and $\frac{(\rho C)_{s,PCM}}{(\rho C)_f} = 0.926$ are non-dimensional parameters for the adopted PCM.

In the present study, the parameter of interest is the Nusselt number, which shows the heat transfer from the wall. The local Nusselt number along the hot wall is written as:

$$Nu = -\left(\frac{\partial \theta}{\partial \mathbf{n}}\right)_D, \tag{30}$$

where D is the total length of the heater where $D = \frac{d}{L}$. The average Nusselt number at the basis of the fin can be introduced as:

$$\overline{Nu} = \frac{1}{D}\int_0^D Nu d\mathbf{n}. \tag{31}$$

The pressure drop across the channel (ΔP) can be obtained as:

$$\Delta P = P_{\text{in}} - P_{\text{out}}. \tag{32}$$

3. Numerical method and validation

The dimensionless governing equations subject to the selected boundary conditions are solved with the Galerkin weighted residual finite-element method. The computational domain was divided into sub-domains (finite elements) (Fig. 2) and each of the velocity distribution, pressure and temperature are approximated by basis set $\{\Phi_j\}_{j=1}^M$ as,

$$\mathbf{V} \approx \sum_{j=1}^{M} \mathbf{V}_j \Phi_j(X,Y), \quad P \approx \sum_{j=1}^{M} P_j \Phi_j(X,Y), \quad \theta \approx \sum_{j=1}^{M} \theta_j \Phi_j(X,Y), \tag{33}$$

Comparison with Küttler and Wall [29] for the case of a square lid-driven cavity as shown in Fig. 3 shows an excellent agreement between the deflections of the flexible base. Fig. 4 depicts additional validation with experimental results of Chakraborty et al. [30] regarding the deflection of a membrane with an externally applied pressure. The figure presents plausible agreement between numerical and experimental results. Thereby, the reliability of the present method is asserted.

4. Results and discussion

Computational outcomes are exhibited within the channel deformation, streamlines, isotherms, local velocity, local displacement, average temperature, average Nusselt number, pressure drop over the entire channel and the skin friction coefficient for various dimensionless times

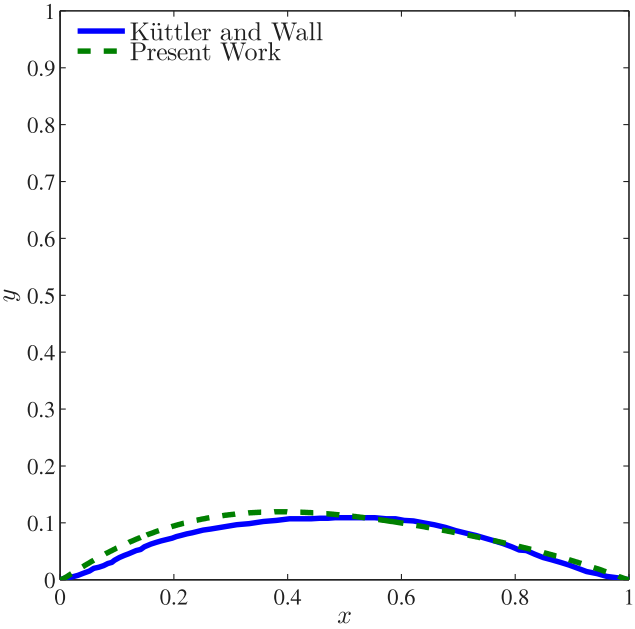

Fig. 3. The deformation curves of the deformable lower bound of the lid-driven enclosure examined by Küttler and Wall [29] and the present study at $\tau = 7.5$ s.

($10^{-1} \le \tau \le 10^{1}$), Reynolds numbers ($10 \le Re \le 500$) and Young's modulus of the elasticity ($10^5 \le E \le 10^8$), while the Prandtl number is fixed at 0.71.

Fig. 5 illustrates the evolution of streamlines with τ for $Re = 100$ and $E = 10^5$. The main purpose to draw this figure is to track the deformation of the two flexible baffles and to indicate the expected time to attain the steady state condition. It can be observed that the increase in τ from $\tau = 0.1$ to $\tau = 20$ leads to the increase in the flow disturbance especially in the middle of the channel. Moreover, a minor vortices begin to construct adjacent to the baffles and their sizes increase with the increase of τ. Also, the strong circulation of the flow inside the channel is responsible for deforming the baffles and making them shake and curved. This is due to the high selected value of the Reynolds number (i.e., $Re = 100$). With respect to the flow pattern, baffles shape and PCM source, it can be noted from the results of Fig. 5 that there is a clear similarity between them for $5 \le \tau \le 20$. Moreover,

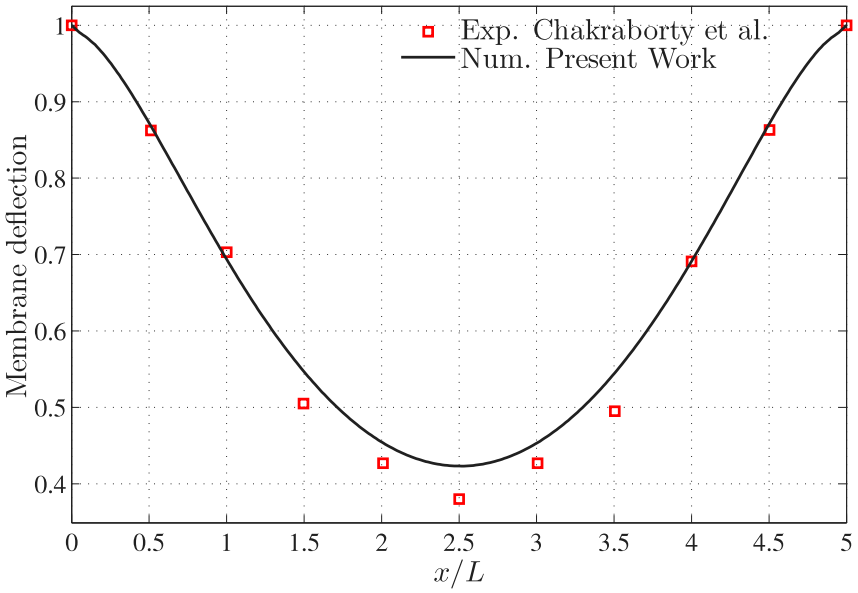

Fig. 4. Comparison of membrane normalized deflection for experimental work of Chakraborty et al. [30] for average velocity of $U = 6.6 \times 10^{-3}$ m/s.

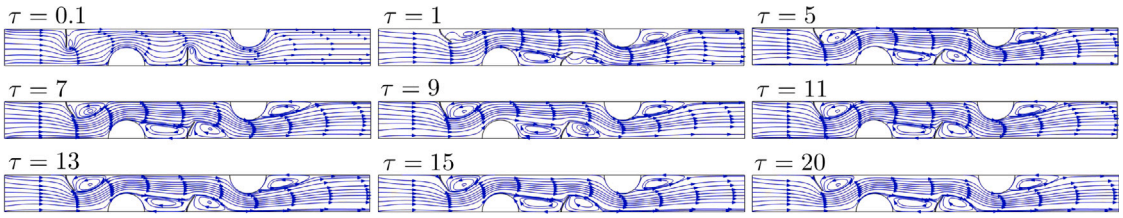

Fig. 5. Variations of the unsteady streamlines evolution by the dimensionless time (τ) for $Re = 100$ and $E = 10^5$.

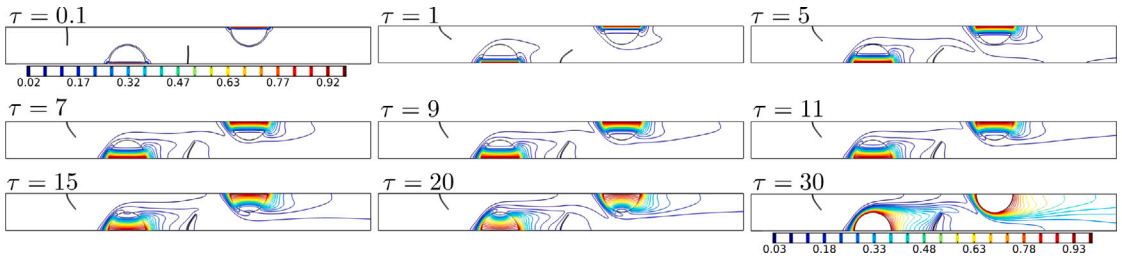

Fig. 6. Variations of the unsteady isotherms evolution by the dimensionless time (τ) for $Re = 100$ and $E = 10^5$.

the steady time which was considered to present the results in the next figures is $\tau = 20$.

The unsteady evolution of the isotherms with τ for $Re = 100$ and($E = 10^5$ was illustrated in Fig. 6. When the value of τ is small (i.e., $\tau = 0.1$), the isotherms are initiated slowly adjacent to the PCM sources in the top and bottom walls of the channel. But, as values of τ increase gradually from $\tau = 1$ to $\tau = 30$, a clear change in the behavior of isotherms was noted. Firstly, they grow with the increase of τ until they reach the exit of the channel at $\tau = 30$. Secondly, the two flexible baffles begin clearly to vibrate with the increase of τ. This vibrating process makes a good mixing between the cold entering fluid and the convection currents originate from the hot PCM attached in the channel walls. Moreover, it can be seen that the PCM begins to melt and a clear disturbance in their pattern can be seen with the increase of τ.

Fig. 7 represents the variation of melt fraction distribution of PCM with time for $Re = 100$ and $E = 10^5$. As time passes, we can easily observe the shape and movement of the melting interface. The red hue indicates that the material is totally liquid ($\tau = 30$ min) and the black color indicates that the material is completely solid ($\tau = 0$ min). The melting front, which divides the liquid and solid regions, is represented by the mushy zone. We can see that during the early stages of the melting process (time= 0 – 30 min), the melting interface is virtually parallel to the bottom wall, indicating that heat transport is primarily by conduction. It demonstrates that the melt fraction grows over time. When the time reaches 30 min, the liquid PCM, which has a greater temperature and lower density, rises and then falls for a significant number of cycles. It can also be seen that melting the top layer of the PCM chamber takes about 20 min. Half of the PCM in the PCM chamber melts in around 10 min.

The variations of steady streamlines (left), isotherms (middle) and melt fraction contours (right) evolution with Re at $\tau = 20$ and($E = 10^5$ were illustrated in Fig. 8. It can be noted that the increase in Re leads to increase in the strength and disturbance of the flow inside the channel. It was seen that, when the Reynolds number is low (i.e., $Re = 10$) the flow pattern inside the channel is uniform and minor vortices of a small size can be seen behind the two baffles. Now, as the Reynolds number increases from $Re = 50$ to $Re = 250$, an obvious confusion in the flow pattern was detected. The streamline contours become closer

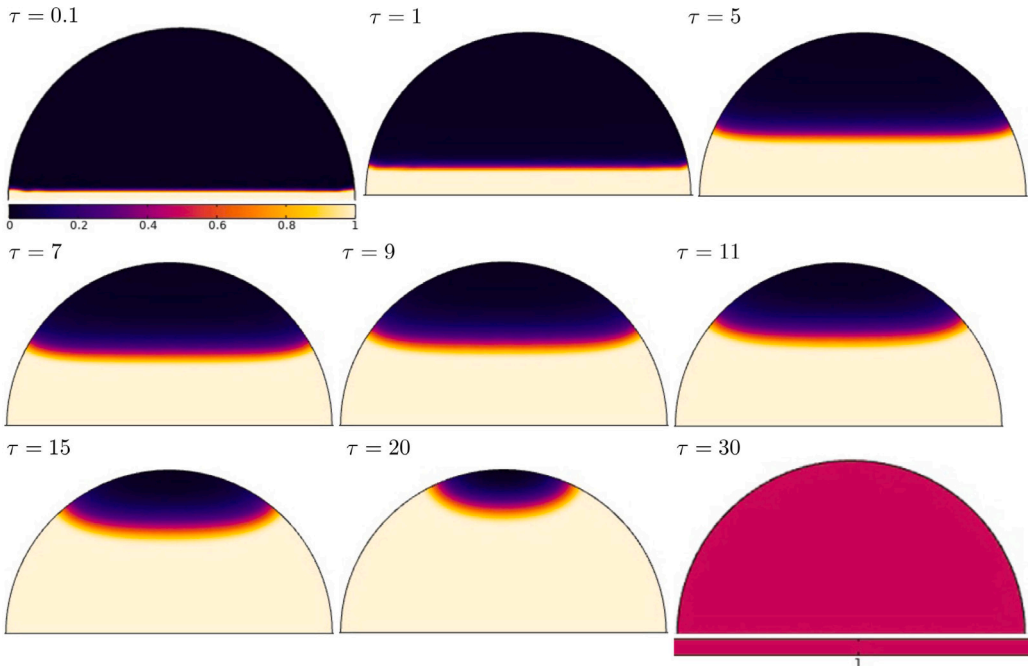

Fig. 7. Variations of the unsteady melt fraction contours evolution by the dimensionless time (τ) for $Re = 100$ and $E = 10^5$.

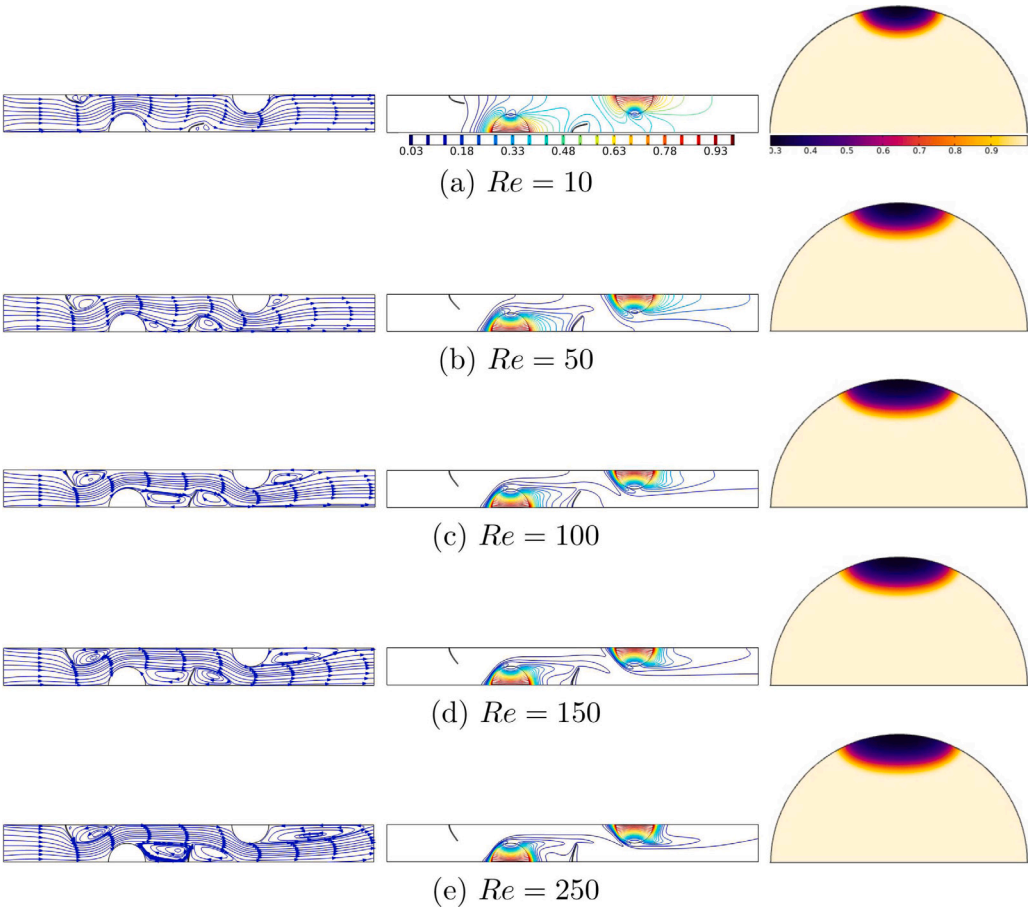

Fig. 8. Variations of steady streamlines (left), isotherms (middle), and melt fraction contours (right) evolution by Reynolds number (Re) for $\tau = 20$ and $E = 10^5$.

to each other especially in the middle of the channel compared with the corresponding contours noted at $Re = 10$ and become very intense at $Re = 250$. In addition, the size of minor vortices adjacent to the baffles begins to grow clearly. Moreover, the increase in Re causes an extra

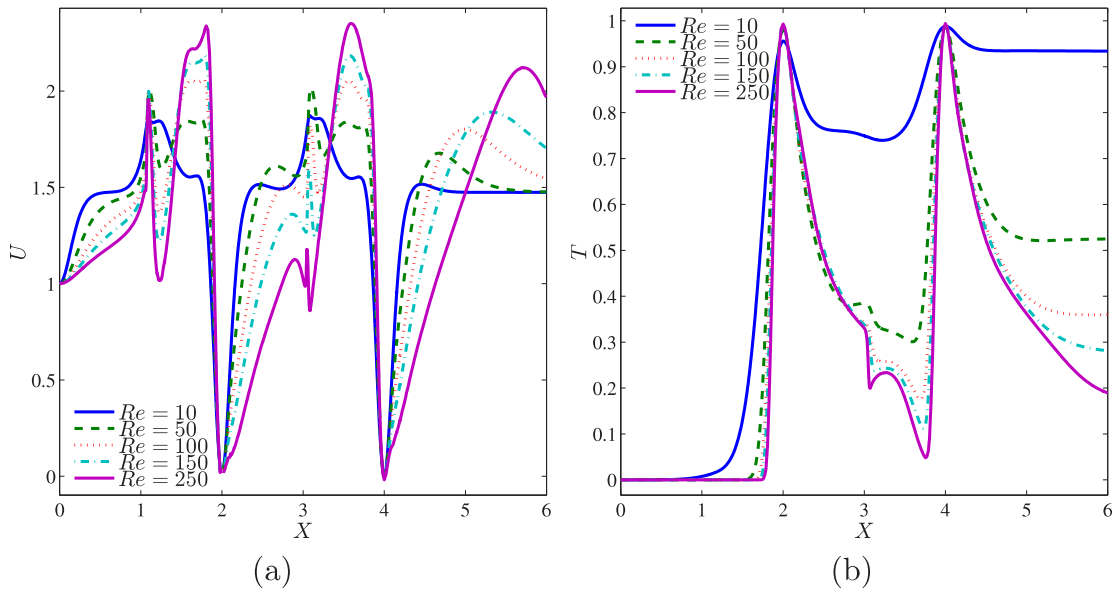

Fig. 9. Variations of (a) local velocity with the horizontal line X at $Y = 0.6$, and (b) local temperature at the bottom flexible baffle for different Re at $\tau = 20$ and $E = 10^5$.

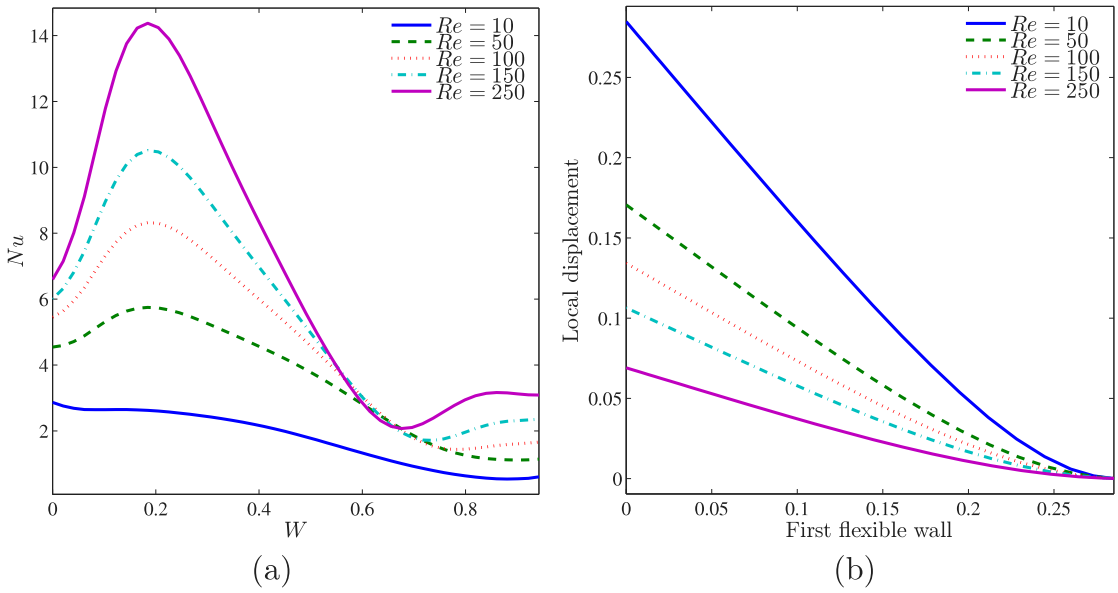

Fig. 10. Variations of (a) local Nusselt number around the first PCM, and (b) local displacement at the first flexible baffle for different Re at $\tau = 20$ and $E = 10^5$.

vortices behind the PCM sources and they get enlarge in size and extend further towards the channel exit with the increase in Re. The reason beyond these behaviors is due to the increase in the forced convection effect with increasing Re. With respect to isotherm contours, it can be seen from the results of Fig. 8 that they are accumulated adjacent to the PCM sources. For $Re = 10$, they are in general uniform, but as Re increases, they become curved, disturbed and extended further towards the exit of the channel. With the increase in Re, the boundary layer adjacent to the PCM sources becomes thinner leading to an enhance in the convection heat transfer.

The Reynolds number, however does not have a significant effect on PCM melting fraction. Because of the laminar region's narrow fluctuation interval and the fluid's residence time in the channel has decreased, a reduction in the duration of air movement and PCM heat exchange is observed. Indeed, increasing the Reynolds number reduces the heat exchange time of the fluid inside the channel and the PCM material by increasing the velocity of the fluid in the channel. The thickness of the boundary layer on the channel side is reduced when the Reynolds number is increased, which significantly improves the convective heat transfer process. These two phenomena have balanced each other out, therefore there is not much of an influence on PCM melting in this regime.

The variations of (a) local velocity with the horizontal line X at $Y = 0.6$ and (b) the local temperature at the bottom flexible baffle for various of Re at $\tau = 20$ and $E = 10^5$ was depicted in Fig. 9. An oscillating behavior can be seen for U variation along X as shown in Fig. 9(a) and this conduct was repeated for all values of Re. As expected, the U attains its maximum value for highest Reynolds number (i.e., $Re = 250$). At $X = 0$, the velocity profiles begin to increase gradually until $X = 1$, after that a cyclic decreasing and increasing behavior up to $X = 6$ is seen. Similar trend can be observed for all values of Re. Furthermore, a three additional notes can be detected from Fig. 9(a). The first one was that U reaches its peak values at $Re = 250$ and $X = 4$. The second was that the positive velocity profile begins to damp gradually until it becomes approximately flat at $Re = 10$ and $X = 3.5$. The last one was that the velocity increases with the decrease in Re for $0 \leq X \leq 1.0$,

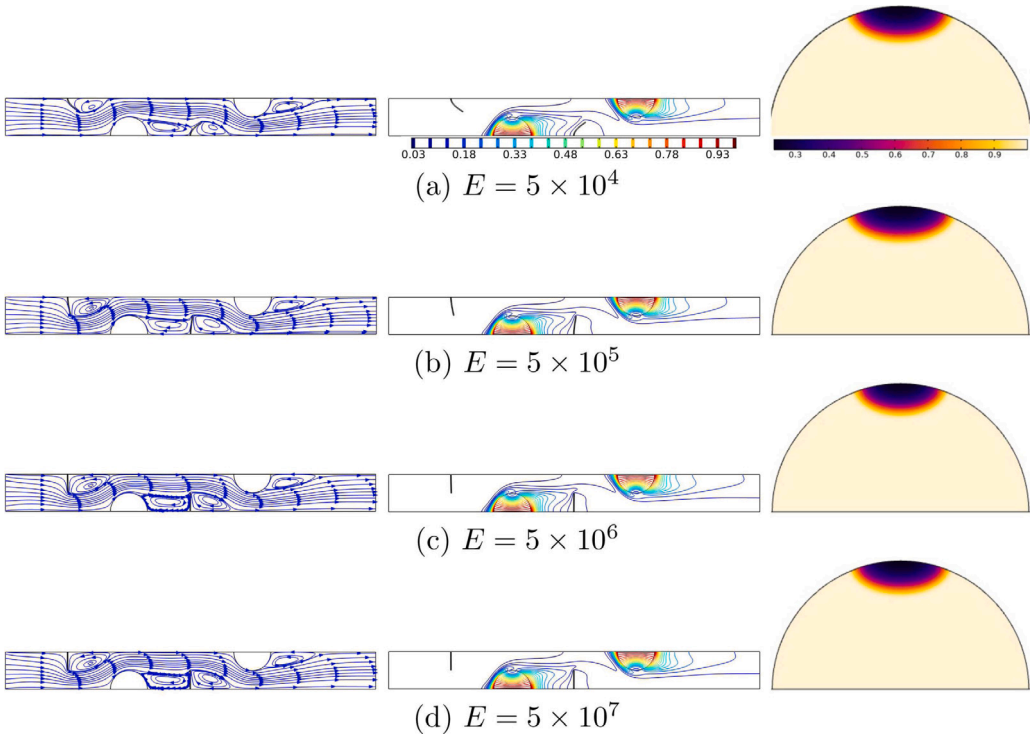

Fig. 11. Variations of steady streamlines (left), isotherms (middle), and melt fraction contours (right) evolution by the elasticity (E) for $\tau = 20$ and $Re = 100$.

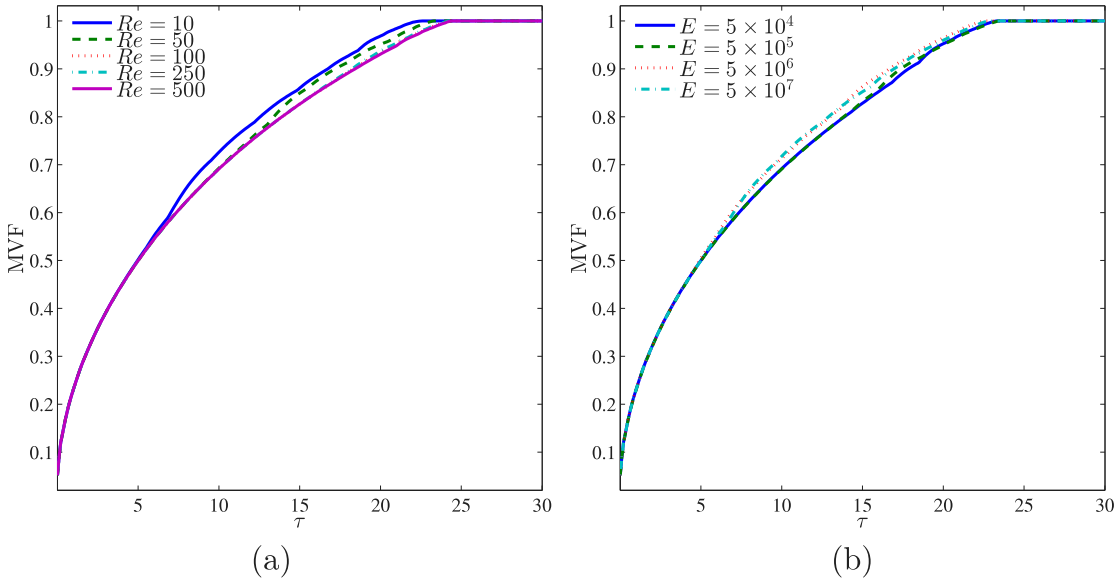

Fig. 12. MVF evolution by various (a) Reynolds number and (b) elasticity with τ.

whereas beyond $X = 4$, low Reynolds number exhibits more uniformity of U velocity. With respect to Fig. 9(b), it can be noted that the local temperature (T) at the bottom flexible baffle remains unchanged for $0 \leq X \leq 1.8$. After that it jumps strongly until it attains its highest value at $X = 2$. Then, it begins to drop again up to $X = 3.8$. For $X = 4$, a similar jump to that found at $X = 2$ repeats itself again until it decreases for the second time at $X = 6$. Also, it can observed from Fig. 9(b) that T decreases with the increase of Re and this is true for all values of X. Moreover, the temperature profiles become less steep at the end of the bottom flexible baffle.

The variation of Fig. 10(a) shows the local Nusselt number around the first PCM source, and Fig. 10(b) portrays the local displacement at the first flexible baffle for various values of Re at $\tau = 20$ and ($E = 10^5$). The results in Fig. 10(a) delineate, in general, that the Nu increases with increasing Re. However, for $Re > 10$, the Nu curves look asymptotical at a critical position of $W \approx 0.65$. The explanation of this critical position refers to that it corresponds to the separation point of the streamlines close to the PCM container and the beginning of the wake. Also, it can be noted that the Nu begins to increase with Re until it attains its peak value at $W = 0.2$ and then begins to decrease. This sudden drop in the Nu can be returned to the flow separation which makes a gap between the channel wall and the flow adjacent to the PCM source. After that, it increases again until it reaches $W = 1.0$. This behavior was repeated at $100 \leq Re \leq 250$. But, at $10 \leq Re \leq 50$ it continues to decrease after $W = 0.2$. With respect to the relation between the local displacement at the first flexible baffle with

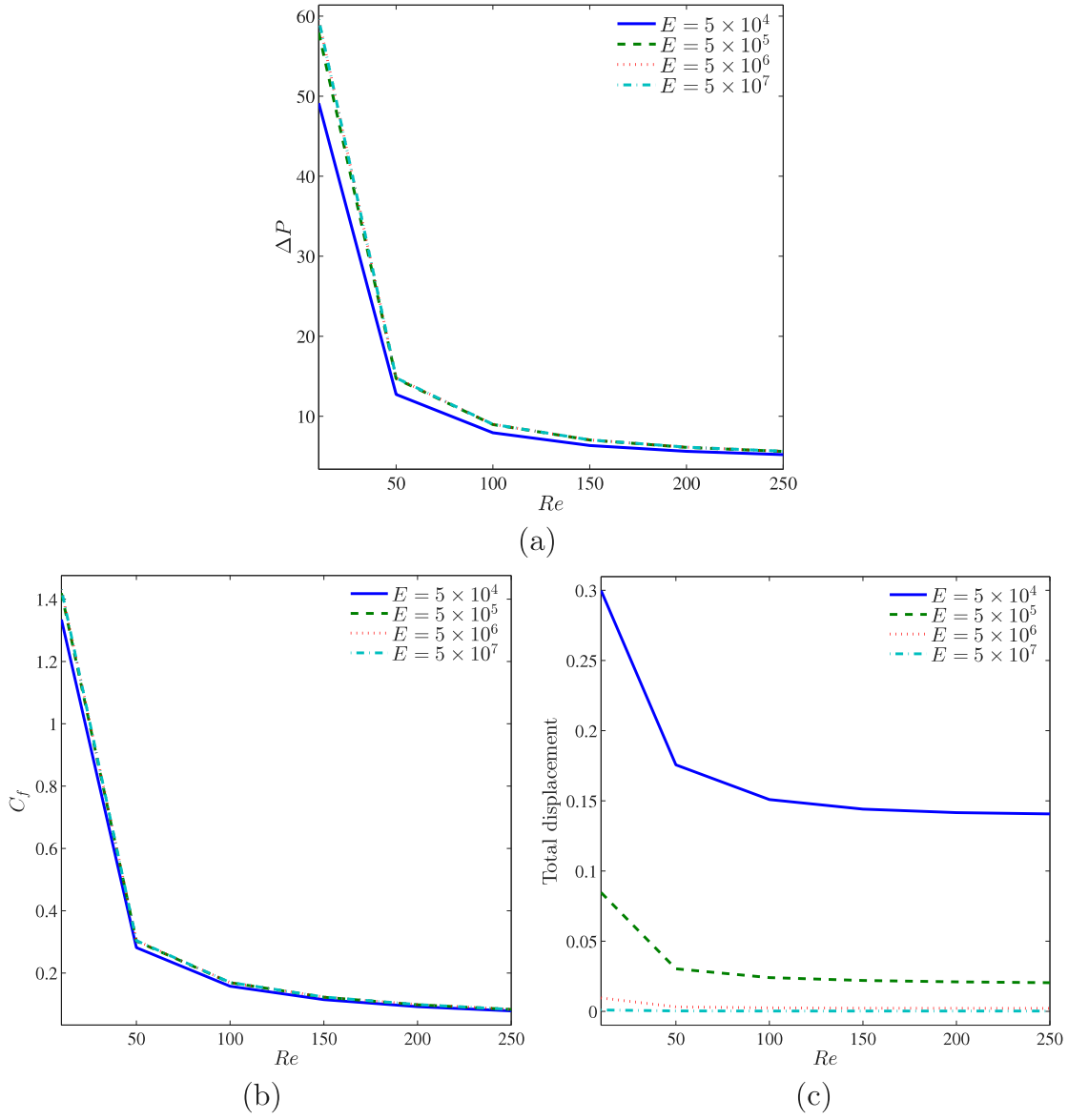

Fig. 13. Variations of (a) pressure drop, (b) skin friction coefficient and (c) total displacement with Re for different E at $\tau = 20$.

Re (i.e., Fig. 10(b)), it was observed that it drops with the increase in Re and length of the first flexible wall.

Fig. 11 illustrates the variations of steady streamlines (left), isotherms (middle) and melt fraction contours (right) evolution with the flexibility parameter E. The latter relates directly to the Young's modulus E^* of the two flexible baffles at $\tau = 20$ and $Re = 100$. It is useful to mention that the Young's modulus or some times called elastic modulus is a measure of the relative stiffness of the material. It relates the ratio between the stress or applied force per unit area to the strain or the deformation (change in the length divided by the original length). It can be noted from Fig. 11, that for low value of flexibility parameter (i.e., $E = 5 \times 10^4$), the deformations of the flexible baffles are high. So, they shake strongly causing an obvious disturbance inside the channel. This gives an extra space for the hot fluid adjacent to PCM source to move faster, decreases the circulation regions and pushes the flow rapidly towards the channel exit. Now, with the increase in E from $E = 5 \times 10^5$ to $E = 5 \times 10^7$, the deformations of the baffles decrease gradually until they return to their straight or stiffer shape at $E = 5 \times 10^7$.

It can therefore be concluded from the streamline contours that the deflection of the flexible baffles against the air flow is very weak for highest flexibility parameter (i.e., $E = 5 \times 10^7$), so a severe wake region can be seen behind the baffles. For the isotherms, it can be seen from the results of Fig. 11 that the increase in E does not have an influential effect on the pattern of them. This can be confirmed from the similarity between the isotherm contours for various values of E. The only exception is that the isotherms behind the second baffle begin to compress with the increase in E. Also, the elasticity of the baffle E has no effect on the PCM melting fraction.

Fig. 12(a) and (b) illustrate the melt volume fraction (MVF) versus time for different Reynolds number at the constant elasticity, and for different elasticity of baffle (E) and for a fixed Re number. As can be seen from Fig. 12(a), along the total melting time, the higher Reynolds number contributes in retarding the melting process. This is because the significant inertial force of the cold air cools the semi cylinders and thus acts against the melting of PCM. Increasing Re from 10 to 500, the reduction in melting volume fraction MVF at $\tau = 15$ is about 4.15%. On the other hand, Fig. 12(b) tells that the baffles having more flexibility (lower elasticity modulus E) gives lesser MVF than rigid (higher E) baffles. The explanation of this trend can be referred to that the bending

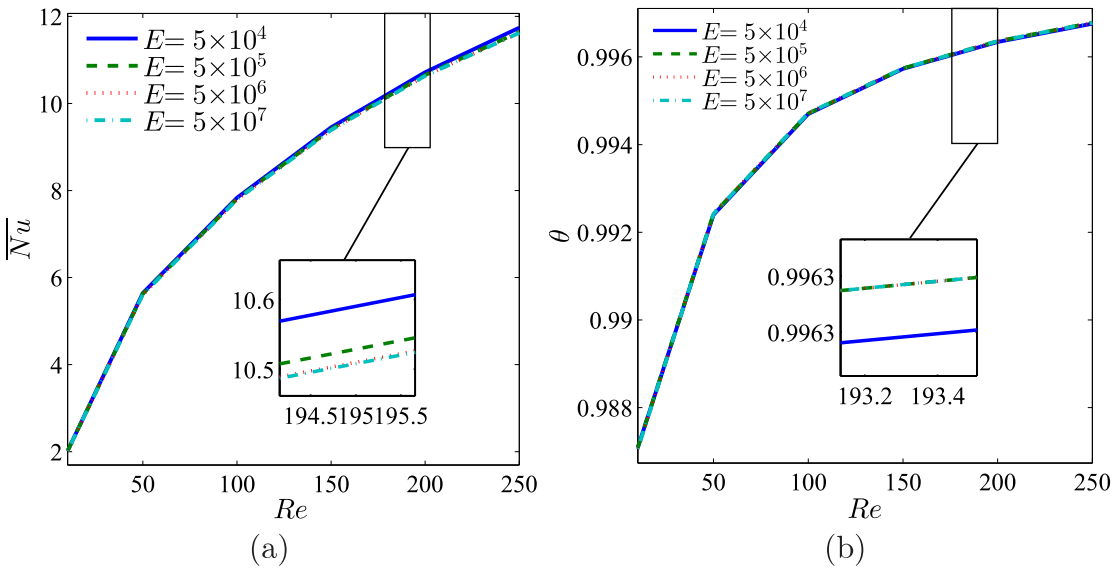

Fig. 14. Variations of (a) average Nusselt number and (b) average temperature with Re for different E at $\tau = 20$.

of flexible baffles provides free passage of cold air to hit the semi-cylindrical enclosures resulting in minimizing the MVF. At $\tau = 15$, the increase in MVF is 5.2% when E is raised from 5×10^4 to 5×10^6.

The variations of Fig. 13(a) pressure drop, Fig. 13(b) skin friction coefficient and Fig. 13(c) total displacement with Re for various values of E at $\tau = 20$ are depicted in Fig. 13. It can be noted from Fig. 13(a), that the pressure drop (ΔP) decreases with the increase in Re. This is due to the decrease in the viscous forces with increasing Re which leads to this reduction in ΔP. It is useful to mention that the decrease in ΔP is very sharp for $Re \leq 50$, whereas its becomes less severe for $55 \leq Re \leq 250$. Also, it can be seen that there is a high matching for the relation between ΔP and Re at $5 \times 10^5 \leq E \leq 5 \times 10^7$. While, it begins to decrease at $E = 5 \times 10^4$. This is a logical result since the decrease in E leads to a decrease in the applied force per unit area or ΔP. The same behavior can be noted again in Fig. 13(b) for the relation between C_f and Re, since C_f begins to decrease with the increase in Re and the decrease in E. The relationship between the total displacement and Re for various values of E is illustrated in Fig. 13(c). It can be noted that the total displacement of the flexible baffles decreases with increasing Re. Also, it decreases with the increase in E until it becomes approximately linear at a highest value of E. Since, when the latter attains its peak value (i.e., $E = 5 \times 10^7$), it increases the applied stress on the baffles and makes the deformation of them are very small.

Fig. 14 shows the variations of (a) average Nusselt number ($\overline{Nu}$) and (b) average temperature (θ) with Re for various values of E at $\tau = 20$. Fig. 14(a) refers that the $\overline{Nu}$ increases with the increase in Re. This is due to the forced convection enhancement with the increase in it. In fact, the existence of the flexible baffles in the channel increases the heat transfer coefficient by increasing the velocity gradient on the baffle head and breaking the boundary layer. This generates high levels of convective currents and enhances $\overline{Nu}$, while, it decreases with the increase in E. This is due to the very weak deflection of baffles which decreases the flow mixing as discussed previously in Fig. 11. From the other side, it was observed also from Fig. 14(b) that the average temperature (θ) increases with Re. This behavior can be seen for all considered values of E. While, the increase in E from 5×10^5 to 5×10^7 has no effect on θ, since it was approximately the same for this range. But, further drop in E to 5×10^4 causes a decrease in θ.

5. Conclusions

From the results we have obtained, the followings can be summarized:

1. The evolution in the dimensionless time leads to an increase in the flow disturbance, especially in the middle of the channel. In addition, it constructs minor vortices adjacent to the baffles and their size increase accordingly.
2. The strong circulation of the flow inside the channel, particularly at a high Reynolds number, is responsible for deforming and shaking the baffles.
3. The evolution in the dimensionless time makes a noticeable change in the isotherm patterns. Moreover, the PCM begins to melt, and an evident disturbance in its pattern can be seen.
4. With the increase of Young's modulus of elasticity, the deformations of the baffles decrease gradually until they return to their straight or stiffer shape at ($E = 5 \times 10^7$). While the pattern of isotherms remains approximately similar, except for the space behind the second baffle.
5. Along the total melting time the higher Reynolds number contributes in retarding the melting process, where increasing Re from 10 to 500, the reduction in melting volume fraction MVF at $\tau = 15$ is about 4.15%. On the other hand, the baffles having more flexibility gives lesser MVF than rigid baffles, where at $\tau = 15$, the increase in MVF is 5.2% when E is raised from 5×10^4 to 5×10^6.
6. The pressure drop, and hence, the skin friction decrease with the increase of Reynolds number and increase with the increase of the elasticity of the baffles.
7. The average Nusselt number increases with Reynolds number, whereas it reduces with an increase in Young's modulus of elasticity. However, the average temperature grows by both Reynolds number and Young's modulus of elasticity.

CRediT authorship contribution statement

Salah M. Salih: Conceptualization, Methodology, Software, Validation, Preparation. **Ammar I. Alsabery:** Visualization, Investigation, Methodology, Writing – original draft. **Ahmed K. Hussein:** Writing – review & editing. **Muneer A. Ismael:** Visualization, Investigation, Methodology, Writing – original draft. **Mohammad Ghalambaz:** Methodology, Writing – review & editing. **Ishak Hashim:** Investigation, Editing.

Data availability

No data was used for the research described in the article.

Acknowledgments

The research of Mohammad Ghalambaz was supported by the Tomsk State University Development Programme (Priority-2030), Russia. We thank the respected reviewers for their constructive comments which clearly enhanced the quality of the manuscript.

References

[1] J.M. Mahdi, S. Lohrasbi, E.C. Nsofor, Hybrid heat transfer enhancement for latent-heat thermal energy storage systems: A review, Int. J. Heat Mass Transf. 137 (2019) 630–649.
[2] J.P. Da Cunha, P. Eames, Thermal energy storage for low and medium temperature applications using phase change materials–A review, Appl. Energy 177 (2016) 227–238.
[3] N. Stathopoulos, M. El Mankibi, M. Santamouris, Numerical calibration and experimental validation of a PCM-Air heat exchanger model, Appl. Therm. Eng. 114 (2017) 1064–1072.
[4] S. Bazri, I.A. Badruddin, M.S. Naghavi, M. Bahiraei, A review of numerical studies on solar collectors integrated with latent heat storage systems employing fins or nanoparticles, Renew. Energy 118 (2018) 761–778.
[5] M. Al-harahsheh, M. Abu-Arabi, H. Mousa, Alzghoul Z., Solar desalination using solar still enhanced by external solar collector and PCM, Appl. Therm. Eng. 128 (2018) 1030–1040.
[6] L.N. Narasimhan, Assessment of latent heat thermal storage systems operating with multiple phase change materials, J. Energy Storage 23 (2019) 442–455.
[7] S.C. Lin, H.H. Al-Kayiem, Evaluation of copper nanoparticles–Paraffin wax compositions for solar thermal energy storage, Solar Energy 132 (2016) 267–278.
[8] M. Bashar, K. Siddiqui, Experimental investigation of transient melting and heat transfer behavior of nanoparticle-enriched PCM in a rectangular enclosure, J. Energy Storage 18 (2018) 485–497.
[9] A. Sciacovelli, F. Colella, V. Verda, Melting of PCM in a thermal energy storage unit: Numerical investigation and effect of nanoparticle enhancement, Int. J. Energy Res. 37 (13) (2013) 1610–1623.
[10] S.M. Salih, J.M. Jalil, S.E. Najim, Experimental and numerical analysis of double-pass solar air heater utilizing multiple capsules PCM, Renew. Energy 143 (2019) 1053–1066.
[11] Z. Liao, C. Xu, Y. Ren, F. Gao, X. Ju, X. Du, A novel effective thermal conductivity correlation of the PCM melting in spherical PCM encapsulation for the packed bed TES system, Appl. Therm. Eng. 135 (2018) 116–122.
[12] R. Jacob, F. Bruno, Review on shell materials used in the encapsulation of phase change materials for high temperature thermal energy storage, Renew. Sustain. Energy Rev. 48 (2015) 79–87.
[13] P. Wang, X. Wang, Y. Huang, C. Li, Z. Peng, Y. Ding, Thermal energy charging behaviour of a heat exchange device with a zigzag plate configuration containing multi-phase-change-materials (m-PCMs), Appl. Energy 142 (2015) 328–336.
[14] X.Y. Li, L. Yang, X.L. Wang, X.Y. Miao, Y. Yao, Q.Q. Qiang, Investigation on the charging process of a multi-PCM latent heat thermal energy storage unit for use in conventional air-conditioning systems, Energy 150 (2018) 591–600.
[15] I. Al Siyabi, S. Khanna, T. Mallick, S. Sundaram, Experimental and numerical study on the effect of multiple phase change materials thermal energy storage system, J. Energy Storage 36 (2021) 102226.
[16] X. Xiao, P. Zhang, M. Li, Preparation and thermal characterization of paraffin/metal foam composite phase change material, Appl. Energy 112 (2013) 1357–1366.
[17] J.M. Mahdi, E.C. Nsofor, Multiple-segment metal foam application in the shell-and-tube PCM thermal energy storage system, J. Energy Storage 20 (2018) 529–541.
[18] B.V.S. Dinesh, Bhattacharya A., Effect of foam geometry on heat absorption characteristics of PCM-metal foam composite thermal energy storage systems, Int. J. Heat Mass Transf. 134 (2019) 866–883.
[19] A. Arshad, H.M. Ali, M. Ali, S. Manzoor, Thermal performance of phase change material (PCM) based pin-finned heat sinks for electronics devices: Effect of pin thickness and PCM volume fraction, Appl. Therm. Eng. 112 (2017) 143–155.
[20] R. Karami, B. Kamkari, Investigation of the effect of inclination angle on the melting enhancement of phase change material in finned latent heat thermal storage units, Appl. Therm. Eng. 146 (2019) 45–60.
[21] J.M. Mahdi, E.C. Nsofor, Solidification enhancement of PCM in a triplex-tube thermal energy storage system with nanoparticles and fins, Appl. Energy 211 (2018) 975–986.
[22] R. Pakrouh, M.J. Hosseini, A.A. Ranjbar, Bahrampoury R., A numerical method for PCM-based pin fin heat sinks optimization, Energy Convers. Manage. 103 (2015) 542–552.
[23] K. Bhagat, M. Prabhakar, S.K. Saha, Estimation of thermal performance and design optimization of finned multitube latent heat thermal energy storage, J. Energy Storage 19 (2018) 135–144.
[24] M. Zukowski, Mathematical modeling and numerical simulation of a short term thermal energy storage system using phase change material for heating applications, Energy Conver. Manage. 48 (1) (2007) 155–165.
[25] G. Verma, S. Singh, S. Chander, P. Dhiman, Numerical investigation on transient thermal performance predictions of phase change material embedded solar air heater, J. Energy Storage 47 (2022) 103619.
[26] P. Promvonge, P. Promthaisong, S. Skullong, Experimental and numerical thermal performance in solar receiver heat exchanger with trapezoidal louvered winglet and wavy groove, Solar Energy 236 (2022) 153–174.
[27] S. Zahran, A.A. Sultan, M. Bekheit, Elmarghany M.R., Heat transfer augmentation through rectangular cross section duct with one corrugated surface: An experimental and numerical study, Case Stud. Therm. Eng. 36 (2022) 102252.
[28] C.S. Wang, C.C. Chen, W.C. Chang, T.M. Liou, Experimental studies of turbulent pulsating flow and heat transfer in a serpentine channel with winglike turbulators, Int. Commun. Heat Mass Trans. 131 (2022) 105837.
[29] U. Küttler, A.W. Wall, Fixed-point fluid–structure interaction solvers with dynamic relaxation, Comput. Mech. 43 (1) (2008) 61–72.
[30] D. Chakraborty, J.R. Prakash, J. Friend, L. Yeo, Fluid–structure interaction in deformable microchannels, Phys. Fluids 24 (10) (2012) 102002.